

Gabor depth migration with topographic seismic data

Yongwang Ma and Gary F. Margrave

ABSTRACT

We present this paper as a complete and final research report on 2D topographic seismic depth migration using the Gabor depth imaging method. This paper demonstrates prestack depth migration results from the *Model 94* synthetic data set, which simulates wavefields recorded on topographic surface after propagating through complex geological structures in the Canadian Foothills. This is also an update on our paper on this topic published in the research report last year.

INTRODUCTION

There are methods available for depth migrations with topographic seismic data. One of these methods, given by Bevc (1997), uses a wave-equation datuming method called ‘flooding the topography’. In this method, the region between a flat datum (above the highest elevation on a topographic surface) and the topographic surface is flooded with a constant (not zero) velocity. Then topographic data are continued upwards, using the wave equation to the flat datum. Then the data can be migrated by a regular imaging method. Another method (Beasley and Lynn, 1992) is called the ‘zero-velocity layer’ method, which sets velocity as zero or a very small value between the flat datum and the topography. Then the algorithm migrates the data from the flat datum. Both of these methods transform recorded topographic data to a flat datum level above the highest elevation of the topographic surface. After the transform is applied to topographic seismic data, regular imaging algorithms are able to work and give correct topographic images.

In other methods, we can modify regular depth migration algorithms and use them to extrapolate wavefields directly from topographic surfaces, where receivers and sources sit, with careful arrangements of seismic data at depth steps (e.g., Reshef, 1991; Margrave and Yao, 2000). The advantage of the second method is obvious. On one hand, the migration process or extrapolation can be started directly from the highest points on the topography instead of the top of the section, at a datum level. As the extrapolation steps down into new depths, receivers on the surface at these depths are added in.

If we use static shifting, final imaging results are always inaccurate. Datuming with a wave equation method gives physical meaning to the process and an accurate image; however, it adds a fair amount of computation to the whole depth imaging process (Beasley and Lynn, 1992), which can always be avoided by using the method of direct extrapolation from topography.

IMAGING TOPOGRAPHIC SEISMIC DATA USING THE GABOR METHOD

In this section, we introduce the details of a method that enables the Gabor depth imaging method to handle wavefield extrapolation from an irregular recording surface. The application of the Gabor imaging algorithms in topographic migration is close to Reshef (1991) and Margrave and Yao (2000), which is called the laterally variable depth step

scheme in this paper. As stated in the previous section, it will not need any datuming or data transform to a flat datum level.

For convenience, we include the formula of the Gabor wavefield extrapolation algorithm for regular seismic data (Ma and Margrave, 2008) here, which is

$$\psi_P(x, \Delta z, \omega) = \sum_{j \in \mathbb{Z}} \Omega_j(x) S_j(x) \int_{\mathbb{R}} \hat{W}_j(k_x, \Delta z, \omega) \hat{\Psi}(k_x, 0, \omega) \exp(-ik_x x) dk_x, \quad (1)$$

where ω is the temporal frequency, k_x is the wavenumber coordinate, and $\hat{\Psi}(k_x, z, \omega)$ is the wavefield at depth z . Wavefield extrapolator \hat{W}_j extrapolates $\hat{\Psi}(k_x, z, \omega)$ to a new depth $z + \Delta z$ as $\hat{\Psi}(k_x, z + \Delta z, \omega)$ (Δz is called the depth step) and is defined as

$$\hat{W}_j = \exp(i\Delta z k_j) = \exp\left[i\Delta z \sqrt{k_j^2 - k_x^2}\right], \quad (2)$$

where $k_j = \omega/v_j$, v_j is the reference (constant) velocity for extrapolation inside partition Ω_j . The wavefield extrapolation using equation (1) is performed in various partitions Ω_j ($j \in \mathbb{Z}$); S_j is known as the split-step Fourier correction in Ω_j (Stoffa et al., 1990). Partitions Ω_j ($j \in \mathbb{Z}$) are important in Gabor depth imaging, they sum to unity along the lateral coordinate so that for all x

$$\sum_{j \in \mathbb{Z}} \Omega_j(x) = 1, \quad (3)$$

where \mathbb{Z} refers to the integer set. A Gabor prestack depth migration uses equation (1) recursively to extrapolate both source and receiver wavefields to any depth, and then compares the fields using an imaging condition to estimate reflectivity.

In recursive depth marching schemes, the key role is played by the wavefield extrapolator \hat{W}_j , which extrapolates the wavefield from depth to depth. An inspection of equation (2) shows that \hat{W}_j is closely related to the depth step Δz . If $\Delta z = 0$, then $\hat{W}_j = \exp(0) = 1$. This relation can be used to specify where the wavefield should be extrapolated in the Gabor imaging method from topography. We set the starting point as a flat datum above all sources and receivers. As a result, there is a region between the flat datum and the topography, where no physical waves are expected to propagate. The seismic wavefields (shot records) should only be extrapolated when the marching depth reaches the topographic surface where data (shot records) are recorded. This is also true for point sources modelled at various source positions. To specify where to extrapolate, we allow the extrapolator depth step, Δz , to vary with lateral position. At a lateral coordinate where the depth level of the marching scheme is above the topography, then extrapolation is not needed, and we set $\Delta z = 0$, and $\hat{W}_j = 1$, meaning no phase-shift will be applied. Otherwise, $\Delta z \neq 0$, and a phase-shift will be performed accordingly using equation (1).

Let $z_t(x)$ be the depth to the topography at lateral coordinate x as measured from the highest point of the topography and Δz_{nom} be the nominal depth step. Assume the

depth marching begins at the highest topographic point and after j steps is at depth $z_j = j\Delta z_{\text{nom}}$, ($j \in \mathbb{Z}$). Then define

$$n_{z_j}(x) = \frac{1}{\Delta z_{\text{nom}}} [z_j - z_t(x)], \quad (4)$$

which is a count of the number of depth steps between the topography and the current depth. Negative $n_{z_j}(x) < -1$ corresponds to the case when the marching depth is above the topography. Then the actual depth step used in our algorithm for step $j + 1$ is given by

$$\Delta z_{j+1}(x) = \begin{cases} 0 & n_{z_j}(x) < -1 \\ [1 + n_{z_j}(x)] \Delta z_{\text{nom}} & -1 \leq n_{z_j}(x) < 0 \\ \Delta z_{\text{nom}} & 0 \leq n_{z_j}(x) \end{cases} . \quad (5)$$

Equation (5) defines the extrapolation step sizes above, on, and below the topographic surface where seismic data are acquired. Figure 1 shows the resulting depth steps on a topographic model that we will use to test the Gabor depth imaging method. With these step sizes well defined, the wavefield extrapolation with phase shift methods, including the Gabor depth imaging method, will be straightforward whether the data are recorded on flat surfaces or topographic surfaces. That is, the extrapolation will be automatically controlled by the step sizes set up according to the topography.

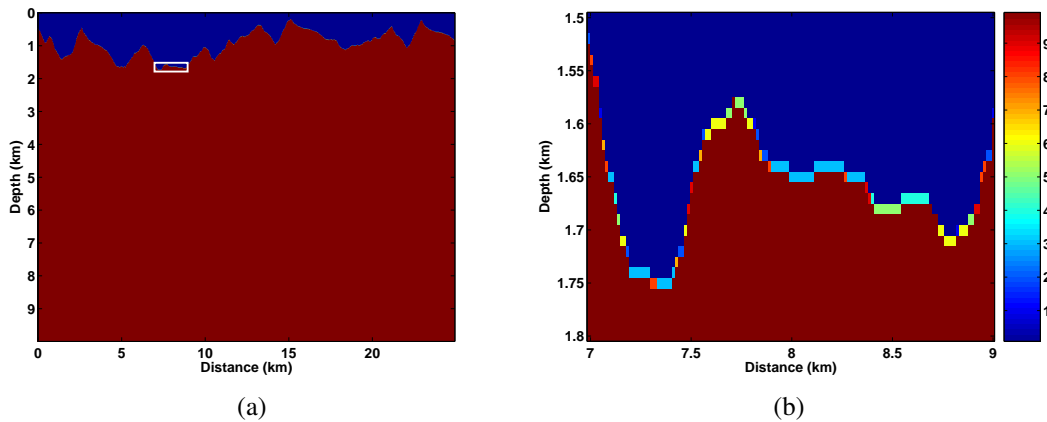


FIG. 1. Step sizes created by equation (5). (a) Laterally variable step sizes for Model 94 topography. (b) Closeup of the region in white box shown in (a). Depth steps are color-coded in m.

GABOR DEPTH IMAGING WITH MODEL 94 DATA SET

Velocity Model

The velocity model is a specific geological model, also known as Model 94 (Gray and Marfurt, 1995), which simulates complex geological structures from the Canadian Foothills. A 2D synthetic seismic data set was created with the velocity model, we use it to test the Gabor depth imaging algorithms designed to image topographic seismic data.

Figure 2 shows the complex velocity structures in the model. The coordinates of the velocity model range from left to right from 0 km to 25 km; and from top to bottom from 0 km to 10 km.

Looking at velocity structures in Figure 2, we see that lateral velocity variations change very rapidly with depth, whether along or below the topography. Depths from 1 km to 6 km, for example, have the most rapid velocity variations in both lateral and vertical directions, which makes wave propagation through them very complicated. We will see the corresponding seismic response in the shot records from topography above this model in the following sections. Also, the relatively low velocities and irregular velocity variations just below the topography will cause a lot of trouble when imaging the structures in the shallow part below the topography. We will get to this point in the following sections, where some initial imaging results will be shown and problems will be presented.

It is always challenging for depth imaging algorithms to reconstruct images with reflection seismic data from a flat surface with such complex velocity structures, let alone seismic data acquired from rapidly changing topography. Therefore, Model 94 is a good model to test how well depth imaging algorithms work when imaging with the data set from topography.

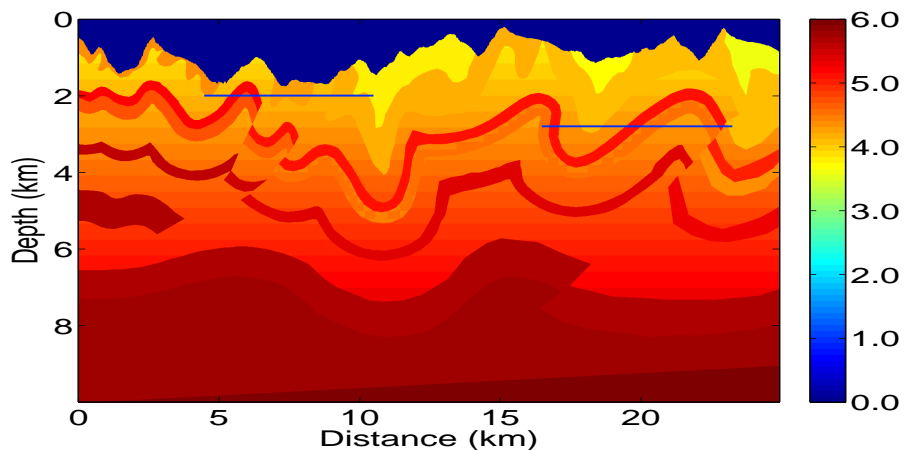


FIG. 2. Model 94 velocity model. Colour bar codes velocities in km/s. The dark blue region along the top of the picture is air with a velocity of 0 km/s. Two blue horizontal lines at about 2 km and 3 km are where the example velocity slices are selected (see Figure 3).

To show lateral velocity variations, velocity slices at different depths from Model 94 are shown in Figure 3 (a) and (b), respectively. These two slices are adapted at certain depths from Model 94, shown in two blue lines superimposed on the velocity model (see Figure 2). Also shown are the adaptive partitions along the lateral coordinate, associated with a given lateral position error (5 m) criterion, using the adaptive partitioning algorithm for the Gabor imaging.

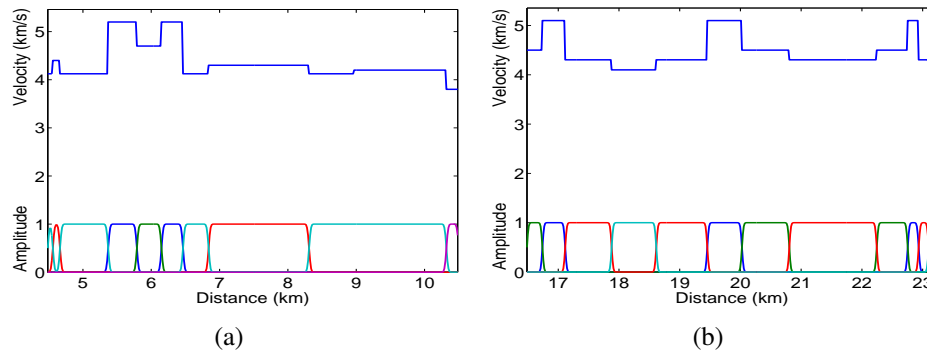


FIG. 3. Velocity slices from Model 94. (a) A slice adapted at a depth of 2 km, from $x = 4.5$ km to $x = 10.5$ km. (b) A slice adapted at a depth of 2.8 km, from $x = 16.5$ km to $x = 23.25$ km. The blue lines on top of (a) and (b) show velocities in km/s. The partitions in the lower parts of (a) and (b) in colours are created by the adaptive partitioning algorithm, corresponding to various velocity segments shown above. Those partitions in both (a) and (b) always sum to 1.

Model 94 synthetic seismic data

Acquisition parameters

Model 94 synthetic seismic data are created with 2D finite-difference modelling (Gray and Marfurt, 1995) using the velocity model introduced in the previous section. 278 shots are excited from the topographic surface, with a shot interval of 90 m. The first shot position is at 0 m with 240 channels, which represents the half spread on the right of the shot. The last shot spread has the half spread on the left containing exactly 240 channels, with shot position at 25 km. Spreads roll in and out from the left to the right and the full spread (both left half and right half) has a maximum of 480 channels in a shot record. Channel interval is 15 m. Each shot advances six stations. Trace length is 2000 samples, with a time sampling rate of 4 ms. The imaging step size in the vertical direction is set to 10 m.

Seismic data from Model 94

Seismic data with topography look different compared to those acquired from the flat surfaces. We can see this from comparing shot records from the Marmousi and the Model 94 data sets shown in Figure 4 (a) and (b), respectively.

From the shot records shown in Figure 4 (b), we can see that some events are ‘crooked’ or ‘folded’ due to the time shift caused by the elevation difference between receivers on a topographic surface, unlike the events in Figure 4 (a), which are close to hyperbolae. These distortions can be also be observed in two other shot records from Model 94, shown in Figure 5. One of them is a full spread containing 480 channels, shown in Figure 5 (b). In the next section, we will set up parameters for Gabor depth imaging and show some imaging examples and analyses of the imaging results.

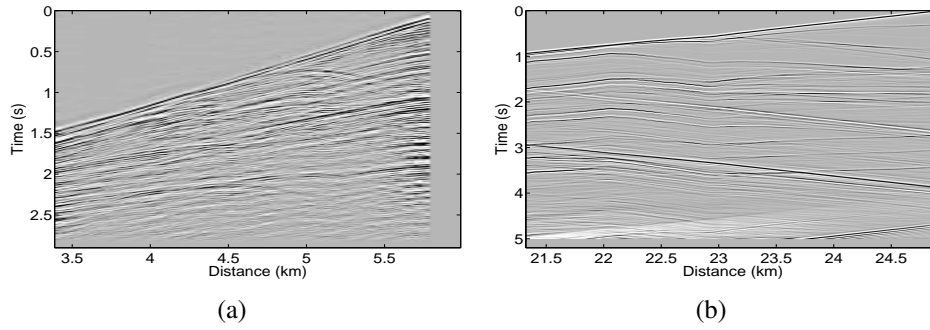


FIG. 4. Seismic data acquired from flat and topographic surfaces. (a) A shot record from Marmousi data set (flat surface). (b) A shot record from Model 94 data set (topographic surface).

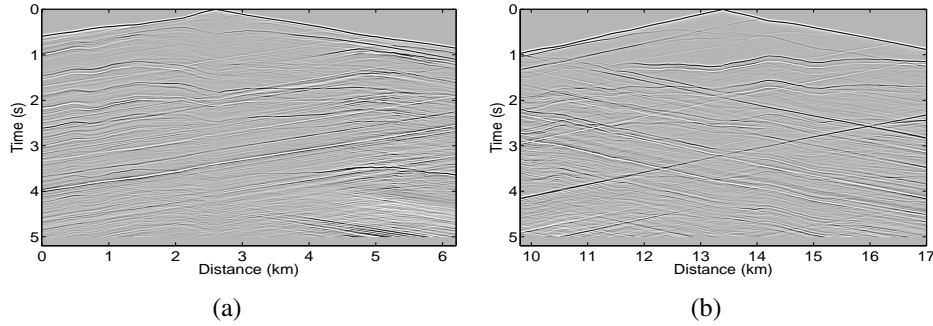


FIG. 5. Two shot records selected from Model 94 data set. (a) Shot record 30. (b) Shot record 150, a full spread containing 480 channels.

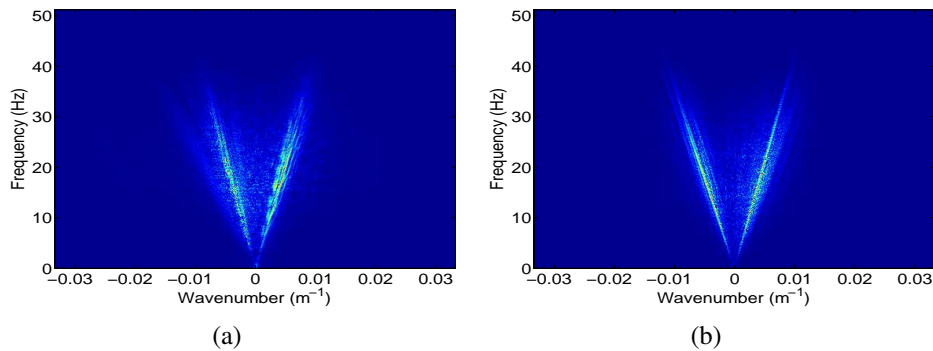


FIG. 6. Selected FK spectra of the shot records from Model 94 data set. (a) FK spectrum of shot record 30. (b) FK spectrum of shot record 150.

Initial imaging results and analysis

Imaging parameters

Since Gabor depth imaging is performed in the frequency-wavenumber (FK) domain, the selection of parameters related to the frequency band and wavenumbers are very important to obtain images of good quality. The (temporal) frequency range of a band-limited wavelet is obtained by the spectral analysis of seismic traces from the Model 94 data set. Two selected FK spectra of the shot records shown in Figure 6 indicate that frequencies above 50 Hz are negligible. Similar conclusions can be drawn from FK spectral analysis on other shot records. Therefore, the maximum frequency for signals in this data set is about 50 Hz. More details can be seen from seismic traces which are Fourier transformed. Some example traces are shown in Figures 7 (a) to (d), where we can reach the same conclusion about the maximum temporal frequency. Also one can see from Figures 7 that the dominant frequency is about 20 Hz. Based on these analyses, an Ormsby wavelet was designed with a frequency range of [3 10 30 50] Hz for seismic source modelling when doing Gabor depth imaging for the Model 94 data set.

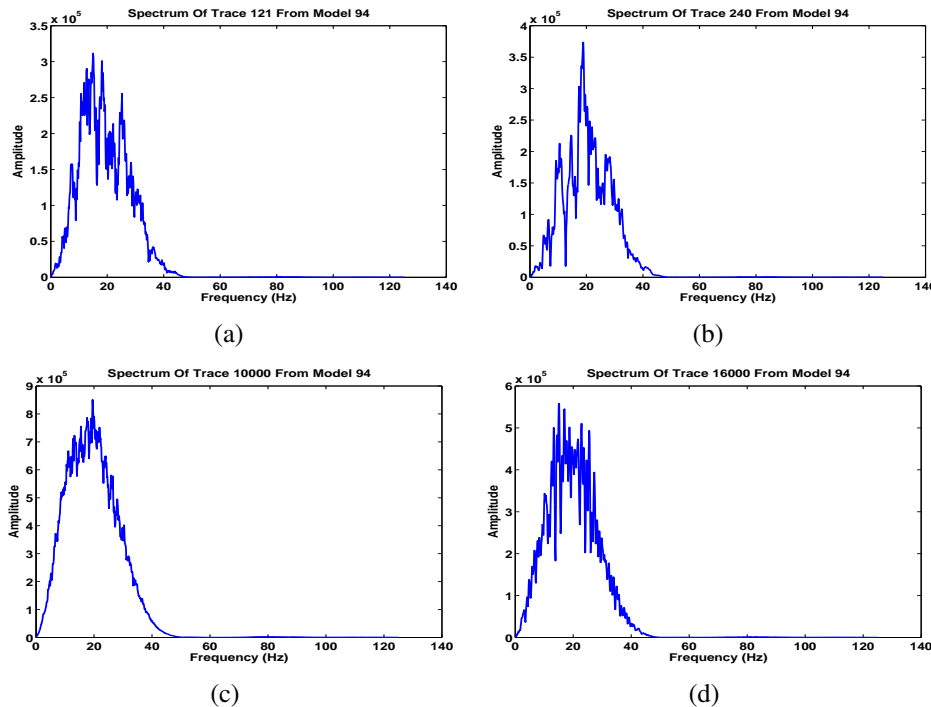


FIG. 7. The temporal spectra of selected traces from the Model 94 data set.

Single shot migrations

First, let us see some single-shot migrations from Model 94. Migrations of the previously mentioned shots 30 and 150 will be used. Gained data and the cross-correlation imaging condition were used in this shot imaging. Figure 8 (a) shows the migration result from shot record 30. Put side by side with it is the reflectivity image for comparison, corresponding to the velocity piece used in the shot migration (see Figure 8 (b)). Figure 8

(c) shows the shot migration of shot 150, and the related velocity piece is also shown as a reflectivity image in Figure 8 (d).

These shot migrations show that one shot may illuminate structures only partially because of the limited aperture from a point source on the surface. However, many such point sources will give sufficient illumination of structures beneath the surface. Stacking all of the shot migrations will help in obtaining the whole picture of those structures. This will be shown in the next section.

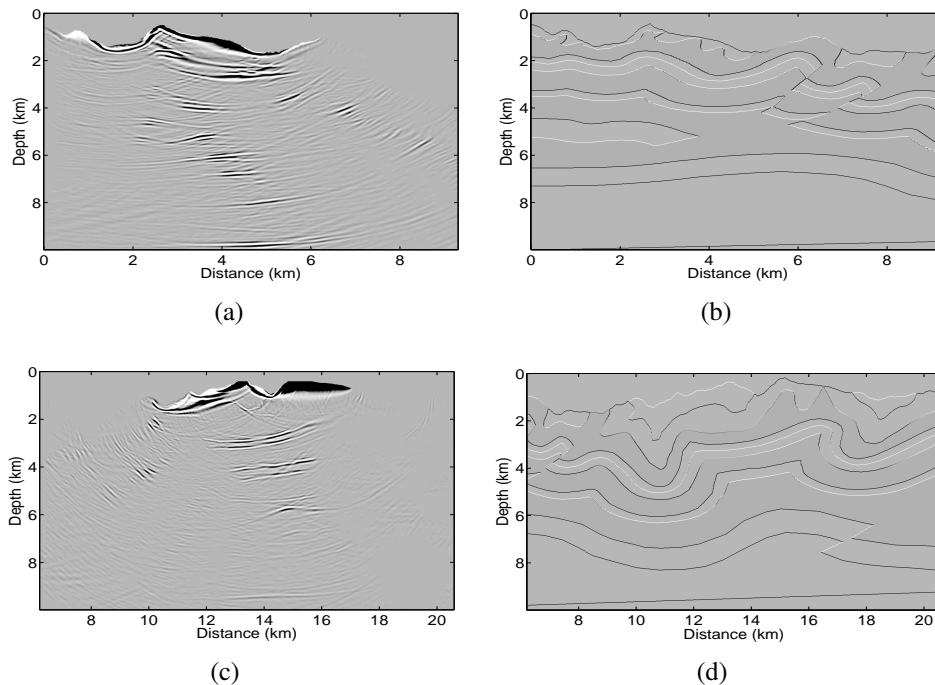
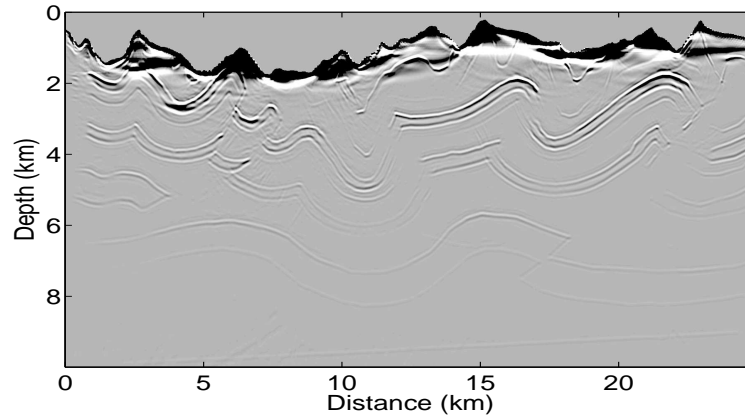


FIG. 8. Shot migrations and reflectivity image pieces. (a) Image with shot record 30. (b) Reflectivity image portion related to shot 30. (c) Image with shot record 150. (d) Reflectivity image portion related to shot 150.

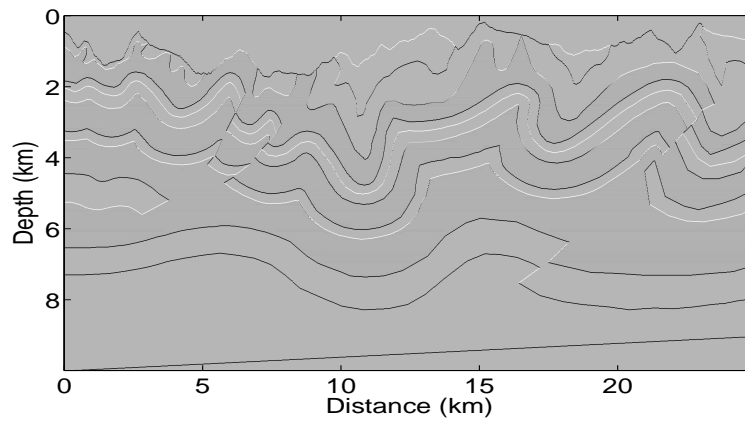
Stacking of all shot migrations

Putting all 278 shot migrations together gives a depth image shown in Figure 9 (a). A reflectivity image of the whole model has been shown in Figure 9 (b) for comparison. Close comparison of the Figures shows that structures deeper than 1.5 km are mostly well imaged. However, the near surface part has been heavily biased by high amplitudes, appearing as black colour, which shades structures in the near surface (just below the topography).

In the next section, we will analyze reasons for the amplitude problems in the image and present methods for removing them.



(a)



(b)

FIG. 9. Model 94 images. (a) Stacking of 278 shot migrations. (b) Reflectivity image.

Problems and solutions in imaging Model 94

There are several possible reasons for the amplitude problems. In the Gabor depth imaging algorithm, evanescent components in wavefields are suppressed (Ma and Margrave, 2008). However, there is still a possibility that these evanescent components can leak into the wave-like region from areas close to the evanescent boundary during the wavefield extrapolation. Therefore, the first reason for the amplitude problem is that evanescent components may creep into extrapolated wavefields during phase-shift operations. The second reason is that if direct arrivals in shot records are included in the imaging, they may be the main contribution for high-amplitude contamination in the near surface image. Another reason are possibly low frequency components in wavefields, which may be amplified when extrapolated near the topographic surface. With these in consideration, we have set up a series of tests to assess these possible causes.

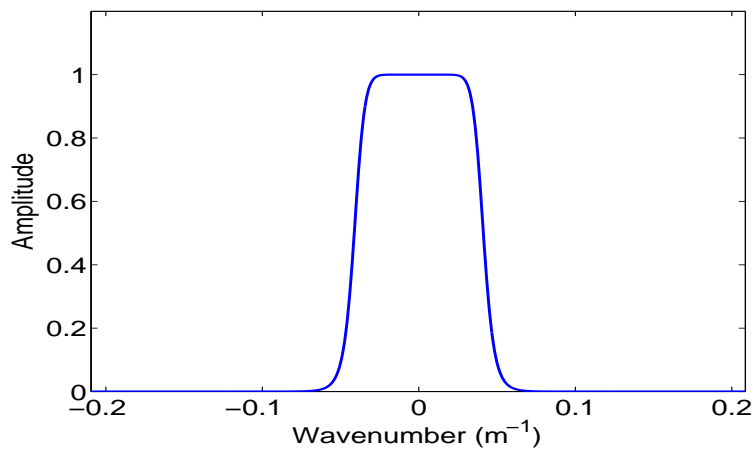


FIG. 10. A wavenumber filter used in the Gabor imaging of Model 94.

In the first test, we use dip filters (or wavenumber filters) in the wavenumber and frequency domain when carrying out the wavefield extrapolation. Figure 10 shows the wavenumber spectrum of one of the filters designed for this imaging test. The boundary of the filter varies with frequencies and wavenumbers, and is defined as a 1D Butterworth filter (e.g., Hale and Claerbout, 1983),

$$f_{dip}(k_x, f, \theta_{\max}) = \frac{1}{1 + \left(\frac{k_x \sin \theta_{\max}}{fv}\right)^n}, \quad (6)$$

where k_x is the transverse wavenumber coordinate, θ_{\max} is the maximum dipping angle, v is velocity, f is frequency and n is the order of the Butterworth filter. Figure 10 shows the shape of the dip filter formulated in equation (6) with $\theta_{\max} = 80^\circ$, $v = 4000$ m/s, $f = 30$ Hz and $n = 12$.

The dip filter is applied to wavefields in a recursive way at depths. Figure 11 (a) shows the depth image from Model 94 using dip filtering defined in equation (6). If one uses visual observation to compare Figure 9 (a) and Figure 11 (a), it would be hard to tell the

difference between the two images. However, the difference between the two images (with and without dip filtering) show something very clear in Figure 11 (b). The dip filters do remove some of the high amplitudes near the surface, i.e. energy that is related to evanescent components during the wavefield extrapolation has been eliminated. However, this image is still not good enough. Therefore, there is a need for another way to further remove unwanted high amplitudes in the near surface image.

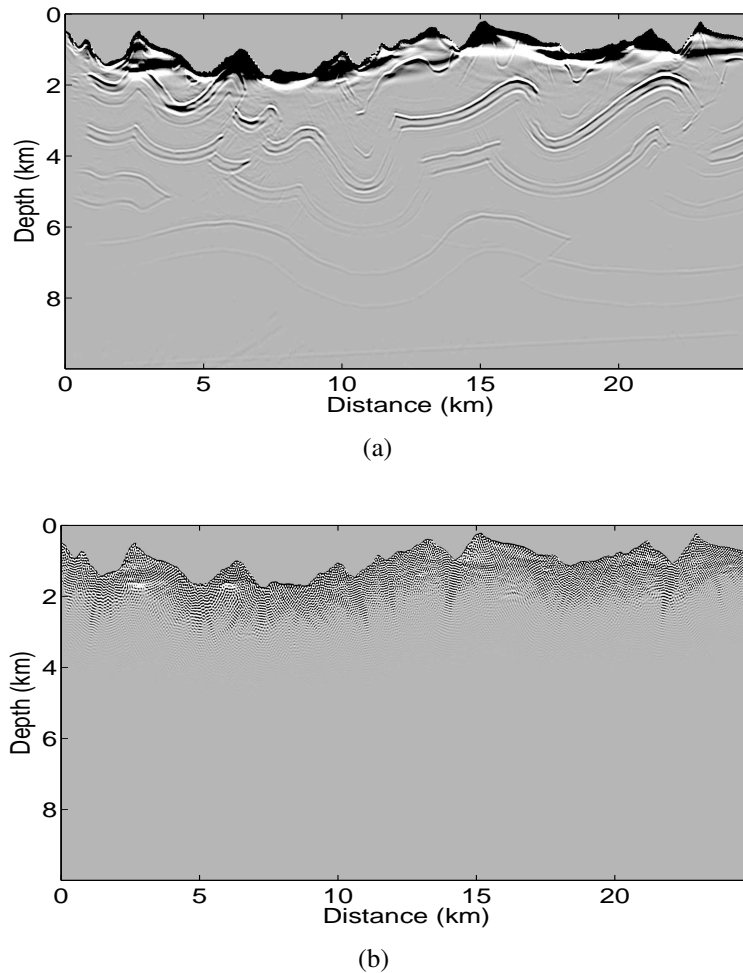
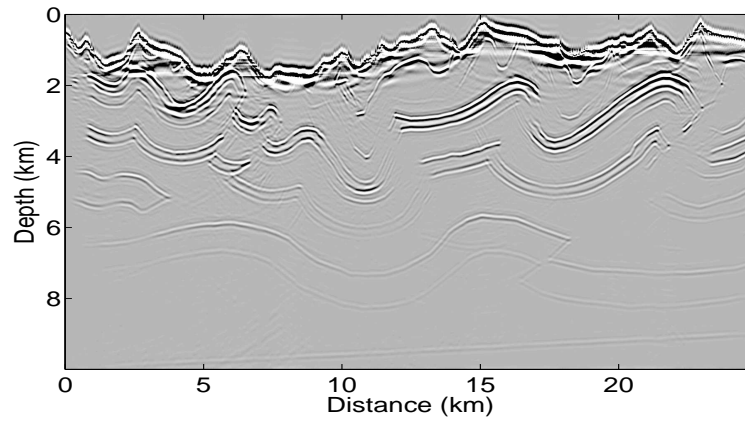


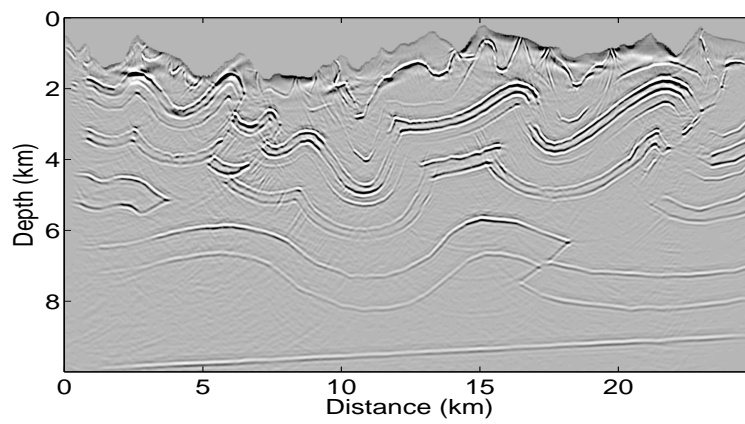
FIG. 11. Dip filtering test in depth imaging of Model 94. (a) Depth image after dip filtering applied. (b) Difference taken between the image in (a) and the one in Figure 9 (a).

The second test is designed to see if high amplitudes are related to low frequency wavefields. A low-cut frequency filtering process on the depth image is given in Figure 12 (a). Comparing with the image in Figure 9 (a), there is improvement in the near surface region after this application. Some structures stand out as the high amplitudes near the surface are filtered out. However, the resolution of the whole image has been lowered, and the structures near the surface still have distortions.

The third test is used to see if direct arrivals contribute to the high amplitude problem. To see this, we have to go back to raw shot records and mute direct arrivals before migra-



(a)



(b)

FIG. 12. Depth imaging of Model 94. (a) Image with low-cut frequency filtering. (b) Image from data with direct arrivals muted.

tion. Shot record 150 demonstrates this. Figure 13 (a) shows the original shot record 150 for comparison. Figure 13 (c) shows shot record 150 with direct arrivals muted. Figure 13 (b) and (d) show the images corresponding to shot records shown in (a) and (c). These two shot migrations show that, when direct arrivals are muted in shot records, the resulting imaging result gets much better. Not only have high amplitudes been removed, showing a better balance in amplitude in the image, but also, some near surface structures shadowed by high amplitudes in the previous shot migrations appear in the image. Comparison between Figure 13 (b) and (d) gives a clear presentation of this.

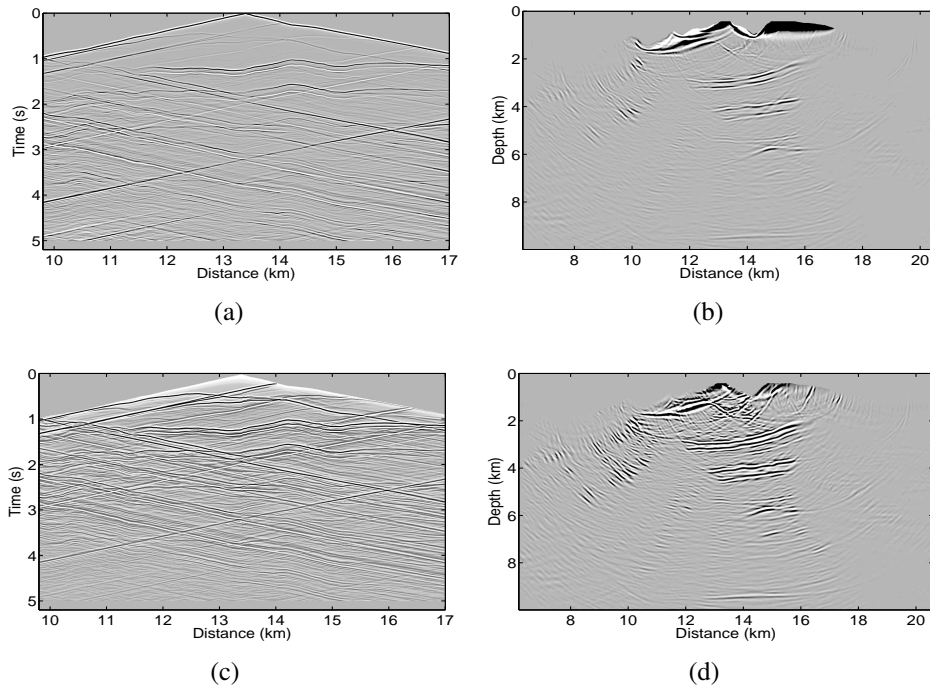


FIG. 13. Test of direct arrival muting in depth migration of shot record 150. (a) Original shot record. (b) Image of shot record in (a). (c) Shot record 150 with direct arrivals muted. (d) Image of shot record in (c).

Figure 12 (b) shows the result of this test on the whole image of Model 94. The depth image quality is much better compared to the old ones (see Figure 9 (a) and Figure 11 (a)). Detailed structures near surface are very clearly imaged, though there still exist little blackish spots and artifacts near the topography.

Final imaging results from Model 94 data set

Based on the analysis and the tests of depth imaging from Model 94, it is suggested that dip filtering and direct arrival muting should be considered when imaging such data sets. To get the best image, we applied a dip filter in the depth imaging of the Model 94 data set with its direct arrivals muted. Low-frequency filtering is not used because it reduces the resolution of the depth image when removing high amplitudes.

Dip filtering and direct-arrival muting together produce the imaging result shown in

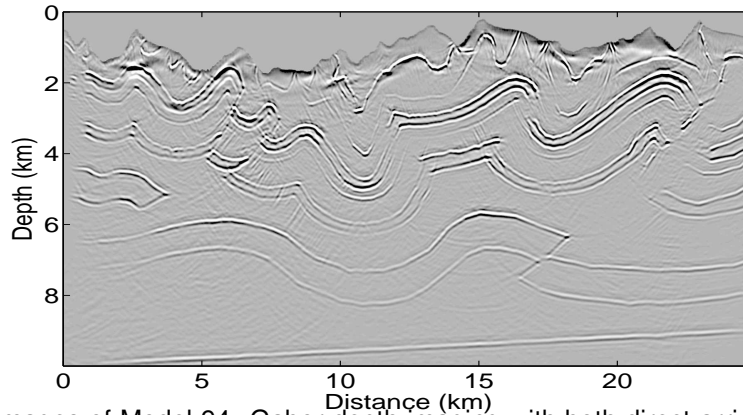


FIG. 14. Depth images of Model 94: Gabor depth imaging with both direct-arrival muting and dip filtering.

Figure 14. The blackish zones disappear in the image near the surface, while the structures in both the shallow and deep parts are still clearly imaged. The most important point is that the shallow structures near the topography appear. Figure 14 shows one of the best imaging results from the Model 94 data set using the topographic Gabor depth imaging method.

CONCLUSIONS

The Gabor depth imaging method has been developed for migrating seismic data from topographic surfaces. This method extrapolates recorded data directly from topography, thus saves computational cost. It gives very clear depth images with the Model 94 data set. The most important improvement of this method is that it can image near surface parts of Model 94 with clear details.

ACKNOWLEDGEMENTS

We wish to thank for financial support of this research from the Consortium of Research in Elastic Wave Exploration Seismology (CREWES) and its sponsors. We also thank the Natural Sciences and Engineering Research Council (NSERC), the Mathematics of Information Technology and Complex Systems (MITACS) of Canada, the Pacific Institute of Mathematical Sciences (PIMS) and the Pseudodifferential Operator Theory in Seismic Imaging (POTSI) for support of various imaging and inversion workshops. We also thank the contributors of the data set used in this paper, Samuel Gray, Gary Maclean and John Etgen, and Han-Xing Lu for helping to remove direct arrivals in the data set. Y. Ma thanks the Canadian Society of Exploration Geophysicists (CSEG) for scholarships, supporting his early Ph.D. studies. Thanks to P. Manning and K. Bonham for reviewing the paper.

REFERENCES

- Beasley, C., and Lynn, W., 1992, The zero-velocity layer: Migration from irregular surfaces: *Geophysics*, **57**, 1435–1443.
 Bevc, D., 1997, Flooding the topography: Wave-equation datuming of land data with rugged acquisition topography: *Geophysics*, **62**, 1558–1569.
 Gray, S. H., and Marfurt, K. J., 1995, Migration from topography: Improve the near-surface image: *Canadian*

- Jorunal of Exploration Geophysics, **31**, 18–24.
- Hale, D., and Claerbout, J. F., 1983, Butterworth dip filters: *Geophysics*, **48**, 1033–1038.
- Ma, Y., and Margrave, G. F., 2008, Seismic depth imaging with the Gabor transform: *Geophysics*, **73**, No. 3, S91–S97.
- Margrave, G., and Yao, Z., 2000, Downward extrapolation from topography with a laterally variable depth step: 2000 Annual International Meeting, SEG, Expanded Abstracts.
- Reshef, M., 1991, Depth migration from irregular surfaces with depth extrapolation methods: *Geophysics*, **56**, 119–122.
- Stoffa, P. L., Fokkema, J. T., de Luna Freire, R. M., and Kessinger, W. P., 1990, Split-step Fourier migration: *Geophysics*, **55**, 410–421.